Published in Physical Review B 58, issue 3, 1300-1317, 1998
which should be used for any reference to this work

Temperature-dependent electronic structure of nickel metal

T. J. Kreutz and T. Greber
Physik-Institut, Universität Zürich-Irchel, CH-8057 Zürich, Switzerland

P. Aebi
Institut de Physique, Université de Fribourg, Pérolles, CH-1700 Fribourg, Switzerland

J. Osterwalder
Physik-Institut, Universität Zürich-Irchel, CH-8057 Zürich, Switzerland

An extended set of temperature-dependent ARUPS data from Ni(111) is presented. The ferromagnetic and the paramagnetic state as well as the phase transition are examined in great detail. Rather new and unconventional modes of data acquisition in ARUPS are applied with high angular and energy resolution, exhibiting great power near the Fermi energy E_F. Even up to $5k_BT$ above E_F energy bands are readily observed. The understanding of these ARUPS data is strongly enhanced by spin-polarized band structure calculations. Exchange-split bands of both, sp- and d-character, are resolved in angular scans and in photoemission Fermi-surface maps. From two-dimensional data sets in energy and angle the dispersion and the exchange splitting are obtained with high precision. All the observed sp- and d-bands clearly exhibit a Stoner-like collapsing-band behavior. The exchange splitting ΔE_{ex} vanishes above T_C in all cases, and ΔE_{ex} closely follows the temperature dependence of the macroscopic magnetization. The apparent deviations from the Stoner-like band behavior stated in P. Aebi *et al.*, Phys. Rev. Lett. **76**, 1150 (1996) are explained. Furthermore we detect anomalously high intensity from a minority d-band close to an sp-band. This strongly suggests that sp-d-fluctuations at the Fermi level are a driving force for the magnetic phase transition of nickel.

I. INTRODUCTION

Nickel is an itinerant ferromagnet, which means that its magnetic moments are carried by the conduction-band electrons. In the ferromagnetic state below the Curie temperature $T_C = 631$ K the conduction electrons in nickel can be divided into two classes: ‘‘spin-up’’ electrons, which have their magnetic moment aligned parallel to a given magnetization direction, and ‘‘spin-down’’ electrons with their magnetic moment antiparallel. The exchange interaction lowers the energy of the spin-up electrons, while raising the energy of the spin-down electrons, giving rise to two slightly different band structures. This leads to the energetic ‘‘exchange splitting’’ ΔE_{ex} between these subsets of electrons, which is of the order of 300 meV and may depend on the energy E, the electron wave vector $\mathbf{k}$, and on the temperature T: $\Delta E_{\mathrm{ex}}(E,\mathbf{k},T)$. Since the affected electronic bands, $3d$ and hybridized $4sp$ states, cross the Fermi level, there are less spin-down electrons than spin-up electrons, giving rise to the names ‘‘minority’’ and ‘‘majority’’ electrons, respectively.

Detailed experimental data on $\Delta E_{\mathrm{ex}}(E,\mathbf{k},T)$ provide an important benchmark for theories on itinerant magnetism. The exchange splitting is a microscopic quantity describing magnetic properties, and it is a local quantity in the sense that the orientation of the magnetic moment can vary from one atomic site to another. When measuring ΔE_{ex} in a photoemission experiment, a macroscopic area on the sample is probed. Therefore macroscopically averaged local information is obtained.

If nickel metal is heated above T_C, the spontaneous magnetic ordering breaks down in a second-order phase transition, leaving the metal in a paramagnetic state. The changes in the electronic structure and the amount of short-range magnetic order (SRMO) above T_C are subjects of a long and still ongoing debate, reviewed in the excellent articles by Capellmann[1] and Donath.[2]

The ground-state properties of nickel can be understood in the Stoner model[3,4] sketched above: majority and minority bands are rigidly shifted against each other and energetically separated by ΔE_{ex}. Finite-temperature predictions of this theory assume that the exchange splitting behaves just like the macroscopic magnetization, which decreases with increasing temperature and completely vanishes at T_C. However, Curie temperatures calculated in the Stoner model are nearly one order of magnitude higher than the experimentally found T_C, and no local magnetic moments are predicted to persist above T_C.

More refined extensions of the Hubbard model, the fluctuating mean-field theories,[5–7] take spin fluctuations into account. Besides cluster calculations[8,9] with regular spin configurations and adjustable small-to-moderate short-range magnetic order (SRMO), there are the disordered local moment (DLM) calculations,[10,11] which assume only uncorrelated transverse and longitudinal spin fluctuations. The most popular of the fluctuating mean-field theories are the local band theories (LBT),[12–14] according to which SRMO and a local exchange splitting can persist above T_C. Transverse spin fluctuations are responsible for the decrease of the macroscopic magnetization at finite temperatures. Whether or not a nonzero ΔE_{ex} exists in the paramagnetic state depends on the group velocity of the electrons. Bands with nonzero group velocity are expected to collapse (‘‘motional narrowing''), while the others may remain exchange split. Yet even in the case of a practically vanishing group velocity, e.g., the Z_2-band investigated in Ref. 15, a collapsing-band behavior can be explained in the framework of the LBT.[16] This makes the experimental discrimination of these theories a very difficult task.

The most recent theory of the magnetism of nickel is the ''generalized Hubbard model.''[17–19] By explicitly incorporating electron-electron interactions and electron-magnon scattering it delivers good values for the ground-state magnetization, the Curie temperature and exchange splittings. And it also reproduces the ''6 eV satellite'' in nickel, which is a many-body effect that occurs when a photoelectron is excited.[20] Moreover, temperature-dependent values of the exchange splittings as a function of wave vector and band index can be calculated. All these values are found to become zero at T_C.

Also from the experimental point of view the finite-temperature band structure of nickel is not well established. Most temperature-dependent ARUPS (angle-resolved ultraviolet photoemission spectroscopy) experiments, with or without spin resolution, show collapsing bands and $\Delta E_{\text{ex}} = 0$ eV at T_C. The three-peak analysis forming the basis for the ''evidence for short-range magnetic order in nickel above T_C'' with a temperature-independent ΔE_{ex} published in Ref. 21 has been shown to rely on a false interpretation of an LBT calculation.[14]

In Ref. 22 spin-resolved ARUPS data in normal emission from Ni(111) were interpreted as showing a strong dependence of the behavior of ΔE_{ex} on the exciting photon energy, i.e., on the location sampled in **k** space. In particular for $h\nu = 16.85$ eV ΔE_{ex} is claimed to remain unchanged when approaching T_C. But the ''complicated line shapes'' measured and fitted for that energy may well arise from several bands, which are simultaneously observed due to the poor angular resolution of $\pm 3°$.[22] So far no clear evidence of a persisting exchange splitting or of some indication of the amount of short-range magnetic order above T_C from ARUPS or IPES (inverse photoemission spectroscopy) experiments has come to the authors' attention.

However, measurements of the angular correlation of (positron) annihilation radiation[23] (ACAR) showed only little changes in the Fermi surface of nickel as a function of temperature, allowing for a reduction of ΔE_{ex} by not more than 30% when going towards T_C. On the other hand, Fermi-surface mapping photoemission experiments[24] revealed drastic differences between room-temperature data and data taken in the paramagnetic state. In spin-polarized electron energy-loss spectroscopy (EELS) data no changes in the spectra were found up to 0.97 T_C.[25] Evidence for spin wave excitations remaining more or less unchanged during the phase transition was given by inelastic neutron scattering experiments,[26] thereby demonstrating SRMO above T_C. Arguments relating the time scales of the various experiments and of the possible spin fluctuations with the observation or nonobservation of a collapsing ΔE_{ex} have been put forward,[1] but will not be discussed here.

It is the primary goal of this paper to present an extended set of high-resolution ARUPS data near the Fermi energy (E_F) in order to settle some of the questions posed by previous experiments mentioned above, and to serve as a benchmark for theories. Rather new and unconventional modes of data acquisition in ARUPS, namely, angular distribution curves, angle-scanned energy distribution curves and constant-energy surface mapping, will be applied (confer Sec. II B). Especially in the vicinity of the Fermi level the new ARUPS modes exhibit their strengths.[27] They even allow one to analyze the thermally excited electronic states *above* the Fermi energy.[28] Instead of combining data from inverse and direct photoemission in order to study the complete set of magnetically active bands, the new data acquisition modes can provide this information in one single experiment. As will be shown, our high-precision data even allow new insight concerning the mechanism driving the phase transition in nickel.

A layer Korringa-Kohn-Rostoker band-structure code[29] has been slightly modified to permit the calculation of band dispersion curves near E_F as a function of energy and of angle, improving the understanding of our data greatly. Thus a very detailed study of the low- and high-temperature properties of nickel and of the magnetic phase transition can be given.

II. EXPERIMENT

A. Sample preparation and characterization

All experiments were performed in a modified Vacuum Generators ESCALAB 220 spectrometer, which is described elsewhere.[30] The Ni(111) crystal was prepared by cycles of 3–5 min Ar^+ sputtering with 800-V acceleration voltage, followed by dosing 24–36 L O_2 and subsequent flashing to approximately 750 °C within about 3 min. During flashing the TDS (thermal desorption spectroscopy) signals of CO, H_2O, Ar, and O_2 were measured to confirm steady-state conditions in the preparation. XPS (x-ray photoemission spectroscopy) with Si $K\alpha$ excitation showed less than 1% oxygen and carbon, no argon and no sulfur. Good surface crystallinity was confirmed by LEED (low-energy electron diffraction) measurements, and XPD (x-ray photoelectron diffraction) data showed good local atomic order and permitted us to measure the crystal orientation to within better than 1°. The ARUPS data were taken with monochromatized He I radiation (21.22 eV) at an energy resolution of about 40 meV and an angular resolution of better than 1° full width at half maximum. Data at high temperatures were taken in a mode with alternating heating and measuring cycles in order to avoid disturbing electric and magnetic fields.[31] Since temperature measurements are only possible with a thermocouple in a sliding contact to the sample holder, a temperature calibration has been made with a thermocouple spot-welded to the sample. Absolute temperature values are precise within 10 K. The Fermi level was determined with an Ag(111) sample at room temperature, taking a spectrum in a direction with no obvious direct transition near E_F. The main contamination limiting the measuring time turned out to be CO adsorbed on the sample surface. At temperatures above ≈ 450 K the CO molecules desorb, enabling longer data taking at elevated sample temperatures.

B. Modes of data acquisition

The most commonly used way to do angle-resolved ultraviolet photoelectron spectroscopy (ARUPS) is to take energy

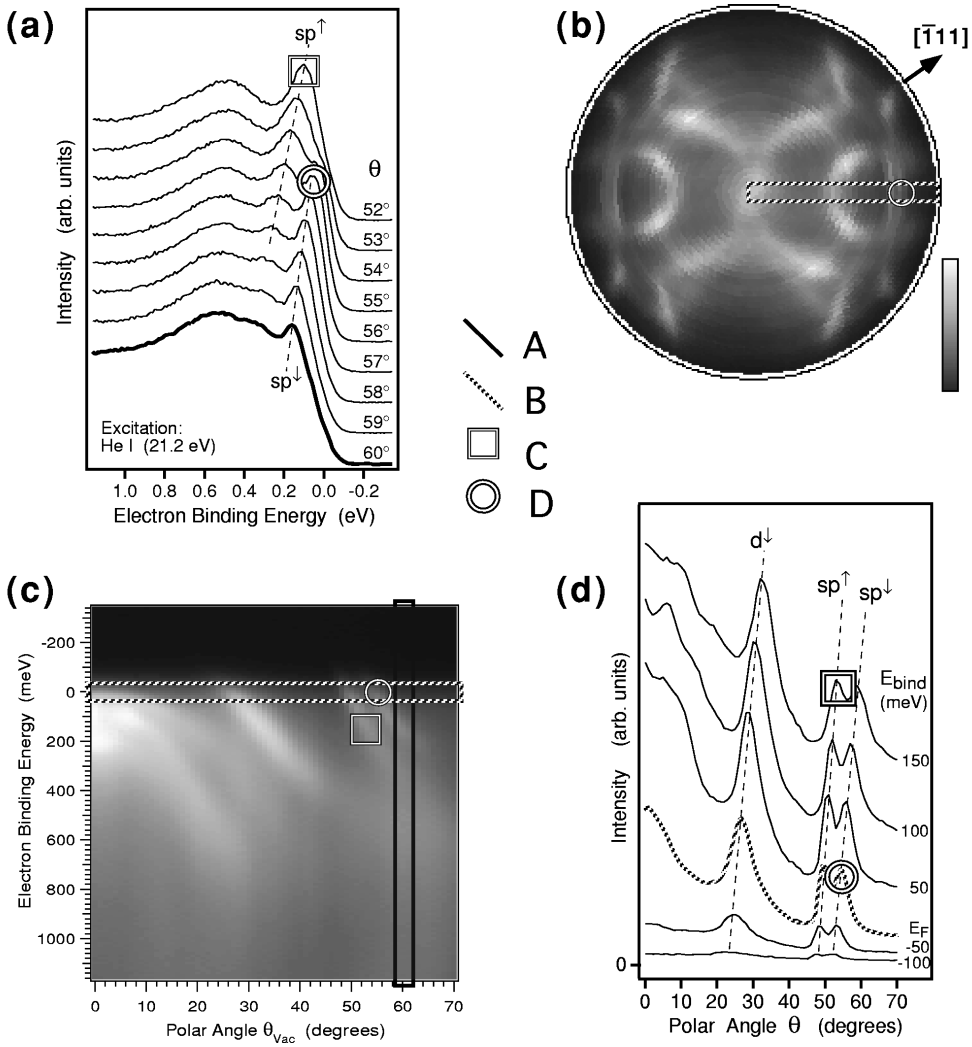

FIG. 1. Illustration of the different modes of data acquisition in ARUPS, which are described in this paper [all data taken at room temperature from a Ni(110) crystal]: (a) Energy distribution curves for various polar angles in the (001) plane; (b) Fermi-surface map; (c) angle-scanned energy distribution curves in the (001) plane; (d) angular distribution curves in the (001) plane. Their relation is illustrated by the following pieces of data: ''*A*'' is the EDC taken at $\theta_{\rm vac}=60°$, ''*B*'' denotes the ADC (polar scan) taken at the Fermi level, ''*C*'' is the $sp^{\uparrow}$ peak at $E_{\rm bind}=150$ meV and $\theta_{\rm vac}=52°$, and ''*D*'' marks the $sp^{\downarrow}$ peak at E_F and $\theta_{\rm vac}=55°$.

spectra, also called *energy distribution curves* (EDCs).[32] For an EDC the experimental geometry is fixed so as to detect only photoelectrons of a certain escape direction given by the polar angle $\theta_{\rm vac}$ and the azimuthal angle ϕ, usually chosen to be a high-symmetry direction. Then the photoelectron intensity is measured as a function of the electron kinetic energy. Peaks in such EDCs usually mark direct transitions from occupied initial states to unoccupied final states.[32]

Given the unique control of the crystal orientation by means of our sample manipulator,[33] we have explored new data acquisition modes for ARUPS. Figure 1 displays examples of these and illustrates their relation. Alternatively to measuring a spectrum of energies for a given electron escape direction one can as well scan the electron escape direction while detecting electrons with a certain kinetic energy, e.g., those from the Fermi level. We term data of this kind ''*angular distribution curves*'' (ADCs) [Fig. 1(d)] in analogy to EDCs. Again peaks indicate the occurrence of direct transitions.

In the case of metals we apply the well-working free-electron final-state approximation. From the dispersion relation for a free electron it follows immediately that the magnitude of the wave vector is given as

$$|\mathbf{k}| = \frac{1}{\hbar}\sqrt{2mE_{\rm kin}},$$

which is constant for a given kinetic energy $E_{\rm kin}$ inside the solid. In $\mathbf{k}$ space this means that the electron final states form a sphere, and in the case of an ADC, they lie on a circle along the angular scanning direction, as shown in Fig. 1 of Ref. 34. Comparison to a Fermi surface calculation allowed to unambiguously identify the involved initial state bands (see also Ref. 24). A clear separation of two exchange-split sp bands was possible without explicit spin detection. It turns out that in this case the effective resolution in the ADCs is superior to that in the EDCs [compare Figs. 1(a) and 1(d)] which reproduce data discussed in Ref. 34.

There are some principal advantages of ADCs over EDCs: (i) bands are detected at the same energy, (ii) this energy can be chosen to be E_F, where lifetime broadening is minimal, (iii) there is no deformation of peaks by the Fermi-

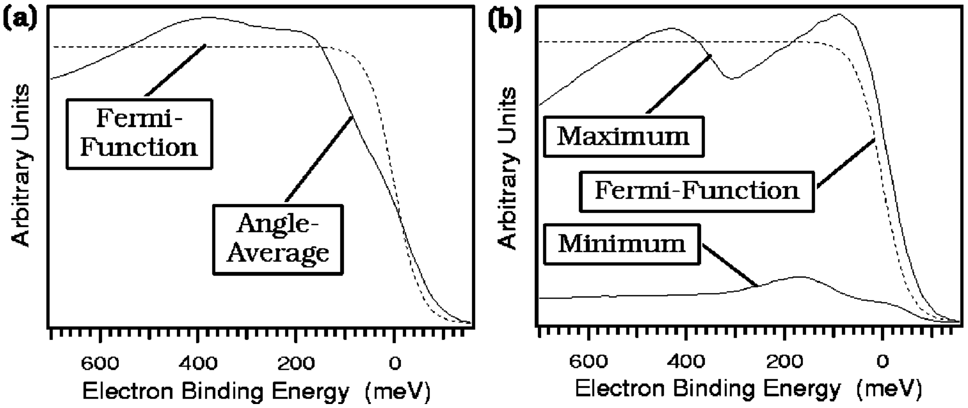

FIG. 2. Examples for the different normalization functions that can be applied to angle-scanned EDCs. In (a) the Fermi normalization function (dashed line) and the average intensity on the ADCs are displayed. (b) compares the Fermi normalization function (dashed line) to the maximum and minimum intensity in the ADCs at the different energies, which are used in the ''maximum contrast'' normalization (see text). Data are taken from Fig. 10.

Dirac distribution, and (iv) transitions can be followed far into the thermally excited tail of the Fermi-Dirac distribution, because angular anisotropies persist above E_F, as will be shown in Secs. III B and III C.

Combining energy distribution curves and angular distribution curves, i.e., taking full EDCs at every angular setting of an angular scan, yields a two-dimensional data set with all the advantages of ADCs, since it also can be viewed as many ADCs at different energies. We term this type of data ''*angle-scanned energy distribution curves*.'' An example is presented in Fig. 1(c). Fitting direct transition peaks in all the ADCs with Lorentzians gives quantitatively the dispersion of the initial state bands as shown in Fig. 5 of Ref. 34. From this it was possible to precisely derive the energetic exchange splitting ΔE_{ex} of the sp band at E_F from the angular exchange splitting $\Delta\theta_{\mathrm{ex}}$.

The amount of information in the thermally excited part of the Fermi-Dirac distribution above E_F is not visible when displaying the raw data in the usual linear grey scale representation. This can be remedied by dividing every EDC by the Fermi-Dirac distribution of the appropriate temperature. In order to avoid overemphasizing background noise in the data points far above E_F a small constant offset of some per mill is first added to the distribution function. If the sample temperature T and the position of the Fermi level are known with sufficient precision and the experimental energy resolution ΔE^{expt} is smaller than k_BT this normalization removes the occupation number of the initial state from the data. This data representation is beneficially used in several figures of this publication.

For data taken at low sample temperatures this normalization becomes unfeasible, since the broadening of the Fermi step due to the experimental resolution ΔE^{expt} is no longer negligible and already small uncertainties in the position of E_F can distort the image around the Fermi level. Nevertheless, if the position of E_F and the experimental resolution function are precisely known and of approximately Gaussian shape, one can still apply the Fermi-function normalization. Numerical simulations have shown that the convolution of the Fermi-Dirac distribution function with a Gaussian peak of a FWHM of ΔE^{expt} yields again, with good accuracy, a Fermi function, where the temperature T has to be replaced by a higher ''effective'' temperature:

$$f_{\mathrm{Fermi}}(E,T)\rightarrow f_{\mathrm{Fermi}}[E,\sqrt{T^2+(\Delta E^{\mathrm{expt}}/4k_B)^2}].$$

At any temperature and without further input the ''angle-average'' normalization can be applied: Every ADC is divided by its average intensity. Also here the angular anisotropies stay unchanged, while the Fermi step is essentially removed.

For a maximum contrast in the data each ADC can be normalized to intensity values ranging from zero to one. This ''maximum contrast'' normalization has to be applied with care, because it sometimes can give misleading results, since the energy dependence of the intensity can be altered strongly. Figure 2 compares the normalization functions for the data set shown in Fig. 10. The curve labelled ''minimum'' (''maximum'') represents the minimum (maximum) intensity value on each ADC, plotted for all the different energies.

The effective removal of the occupation numbers given by the Fermi function allows one to follow the data far into the tail of the distribution function, since the human eye can still recognize very faint and noisy features in these two-dimensional data sets with the aid of the dispersion. Clear identification of transitions up to about $5k_BT$ above E_F will be shown in Secs. III B and III C.

Besides measuring angular distribution curves, i.e., keeping the azimuthal angle ϕ fixed while scanning the polar angle θ or vice versa, it is as well possible to vary both angles while detecting photoelectrons of a given energy. This way a *constant-energy surface map* comprising information on a continuous two-dimensional part of $\mathbf{k}$ space can be mapped by means of photoemission, and in particular Fermi-surface maps can be obtained. The Fermi surface is of special importance, because it determines many properties of a solid, like the electrical and the thermal conductivity, and the chemical behavior. This is due to the fact that electrons at the Fermi edge can pick up and supply arbitrarily small amounts of energy, whereas the more strongly bound electrons are confined by the Pauli exclusion principle and therefore need high excitation energies. Also the ''magnetic bands'' in itin-

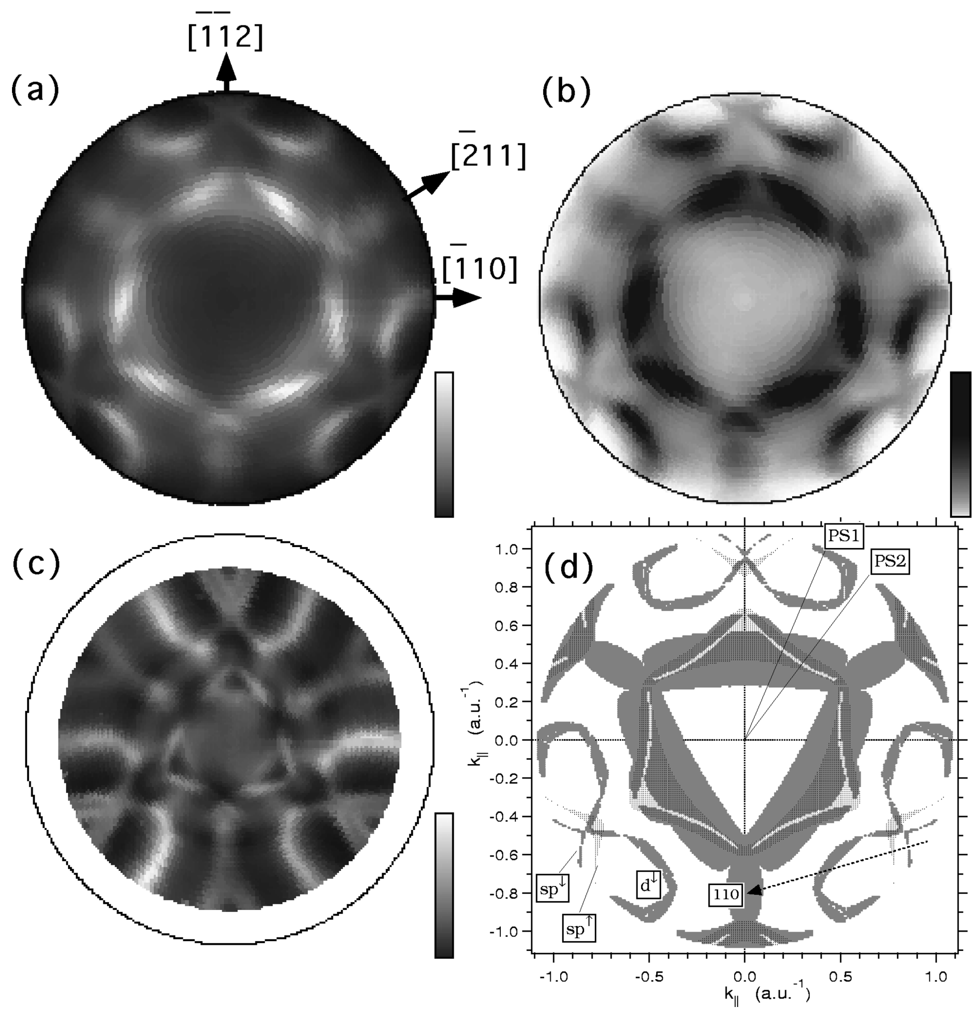

FIG. 3. He I-excited Fermi-surface map from Ni(111). In (a) and (b) the raw data are presented in parallel projection. In (a), high intensities are shown in white, while in (b) the grey scale is inverted with slightly enhanced contrast. (c) shows the data in stereographic projection and normalized with ''ϕ average'' (see Sec. II B). In (d) the corresponding LKKR calculation is displayed. ''PS1'' and ''PS2'' indicate the direction of the angle-scanned EDCs from Sec. III C, Figs. 9 and 10, respectively. The dashed arrow tagged ''110'' roughly follows the line in **k** space corresponding to the polar scan on Ni(110) discussed in Ref. 34.

erant ferromagnets, responsible for the magnetic properties, are, per definition, located close to E_F.

The first photoemission Fermi-surface map has been measured by Santoni and co-workers[35] presenting the Fermi surface of quasi-two-dimensional graphite. The first measurement in this manner, applied to a three-dimensional electronic system, namely, copper, has been given in Ref. 36. The explanation of these data in terms of sections through the Fermi surface and by means of the free-electron final state approximation was given by Aebi *et al.*, published in Ref. 27 together with further measurements and band-structure calculations confirming the interpretation.

The Fermi-surface data are usually presented in a two-dimensional grey scale plot in parallel projection, i.e., the radius at which an intensity is plotted is proportional to $k_\parallel = |\mathbf{k}_f^{\text{vac}}|\sin\theta_{\text{vac}}$, where θ_{vac} is the measured polar emission angle [see, for example, Fig. 1(b)]. Note that due to the inner potential there is a strong refraction effect leading to a smaller polar angle inside the crystal. Alternatively the stereographic projection can be used. There the radius is proportional to $\tan(\theta_{\text{vac}}/2)$. This second presentation is no longer linear in $k_\parallel$ and is used to emphasize fine structure at higher polar angles. Figure 3(c) (Sec. III A) shows an example of a stereographically projected Fermi surface map. Experimentally the intensities often decrease at higher θ_{vac} due to the instrumental response function. In such cases the data can be normalized in order to discover features that might be hidden in the limited dynamic range of the grey scale. The ''ϕ average'' normalization works completely analogously to the ''angle-average'' normalization described before: For every polar angle the intensities on the corresponding azimuthal circle are divided by the average intensity on that azimuthal scan. However, data representations in this normalization have to be regarded with care, because some features may be altered notably. In particular any circular feature recorded near the surface normal will be lost due to the changed polar dependence. For a comprehensive discussion of Fermi-surface mapping see also Ref. 37.

III. RESULTS AND DISCUSSION

A. Fermi surface from Ni(111)

In this section Fermi-surface maps as measured through the Ni(111) surface are presented and compared to band-

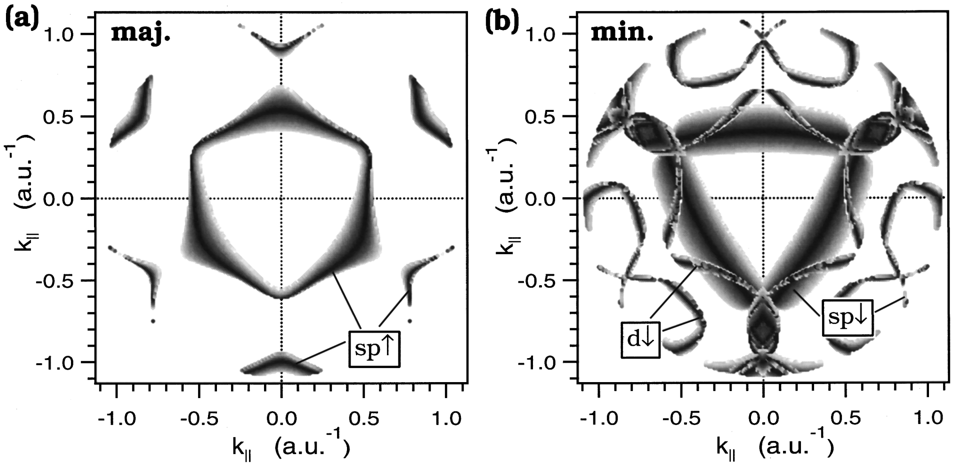

FIG. 4. LKKR calculation for the He I-excited Fermi-surface map taken from Ni(111). (a) majority spin, (b) minority spin. Further information is given in the text.

structure calculations. A layer Korringa-Kohn-Rostoker (LKKR) code as implemented by MacLaren and co-workers[38] has been modified to allow the calculation of Fermi surfaces as measured by photoemission under the assumption of a free-electron final state (compare Ref. 27 and Ref. 24).

The experimental data were taken from $\theta_{\mathrm{vac}}=78°$ up to the surface normal in steps of 2°, containing altogether 5404 angular settings. In Figs. 3(a) and 3(b) the raw data are presented in parallel projection. The grey scale is inverted with slightly enhanced contrast in (b). Figure 3(c) shows the data normalized with ''ϕ average'' and in stereographic projection (confer Sec. II B) in order to emphasize bands that occur at large polar angles. Well-defined bands are readily found in the experimental data. Finally in Fig. 3(d) the corresponding spin-polarized LKKR calculation is presented in parallel projection. The free-electron final-state approximation has been made, assuming an inner potential of 10.7 eV (Ref. 39) and a work function of $\Phi=5.22$ eV.[40] More lightly dotted regions indicate majority spin, and the regions in darker grey stand for minority electrons. Regions of overlap appear darkest.

In Fig. 4 the two spins are displayed separately in grey scale. The darker the dots the better the agreement of the calculated $k_{\perp}$ eigenvalue with the $k_{\perp}$ expected for a free-electron final state (the LKKR code[38] provides all possible $k_{\perp}$ eigenvalues for a given $k_{\|}$ and a given energy). A maximum deviation of 0.1 a.u.$^{-1}$ was allowed for calculated $k_{\|}$-E_{bind} pairs to appear in Fig. 3(d) and in Fig. 4. The binding energy is $E_{\mathrm{bind}}=0$ eV here, corresponding to the Fermi energy. Not only the exact position of the bands can be deduced from the plots, but in Fig. 4(b) the minority *d* and *sp* bands are distinguishable.

Comparing the experimental data with the LKKR calculation shows a rather good agreement as all the measured bands also appear in the calculation. The major differences are intensity variations. Those are predominantly due to photoexcitation matrix elements and polarization effects that the bulk band-structure calculation does not take into account. The latter even give rise to a slight intensity asymmetry around the [1 12] direction. Photoemission calculations might help to quantitatively understand these phenomena.[41] It should be noted here that in the experiment the sample is rotated, which leads to constantly changing polarization conditions inside the crystal lattice. Another deviation between calculation and experiment is in the $k_{\|}$ scale, which appears to be slightly stretched in Fig. 3(d). In particular the *sp* bands near the [1 12] azimuth occur closer to grazing emission ($\theta_{\mathrm{vac}}=90°$) than in the calculation. A different choice of V_0 and/or Φ usually allows one to overcome such discrepancies.[42] The free-electron final-state model employed in the calculations might also be a source of inconsistency.

For high polar angles and near the $[\overline{11}2]$ direction the exchange-split pair of *sp* bands can be found in the experiment. Especially in the stereographically projected data in Fig. 3(c) the clear angular separation of the two is obvious. In Ref. 34 the *sp* splitting was examined at practically this same location in **k** space, using the Ni(110) crystal: The dashed arrow in Fig. 3(d) tagged ''110'' roughly sketches the angular positions on the (111) surface that correspond to the polar scan measured on Ni(110). The arrow head points approximately to the location accessed in normal emission from the (110) face (compare also Fig. 1 of Ref. 24).

As demonstrated in Fig. 1 of Ref. 34 this position is close to the *X* point. In Fig. 4(b) there are obviously several minority bands crossing the Fermi level near that point. The calculation of an angle-scanned EDC-type data set along [211], analogous to calculations that will be discussed in Sec. III C, revealed that besides the two exchange-split *sp*-like bands, there are another three minority bands of *d*-like electrons to be expected. All these bands cross the Fermi level twice between normal emission and $\theta_{\mathrm{vac}}=90°$, summing up to 10 Fermi level crossings altogether. Despite this complicated situation some fine structure along the [211] direction allows one to clearly distinguish two different bands in the experiment. According to the LKKR calculation these are minority *d* bands, and consequently not even an explicitly spin-resolved PES experiment could help to disentangle the complicated situation near the *X* point.

In Ref. 24 the Fermi surface of nickel as measured through the (110) surface is discussed. Only room-temperature data and data at $1.1T_C$ were presented. The evolution with the temperature can be found in Ref. 43. We now want to extend these studies to Fermi-surface maps measured

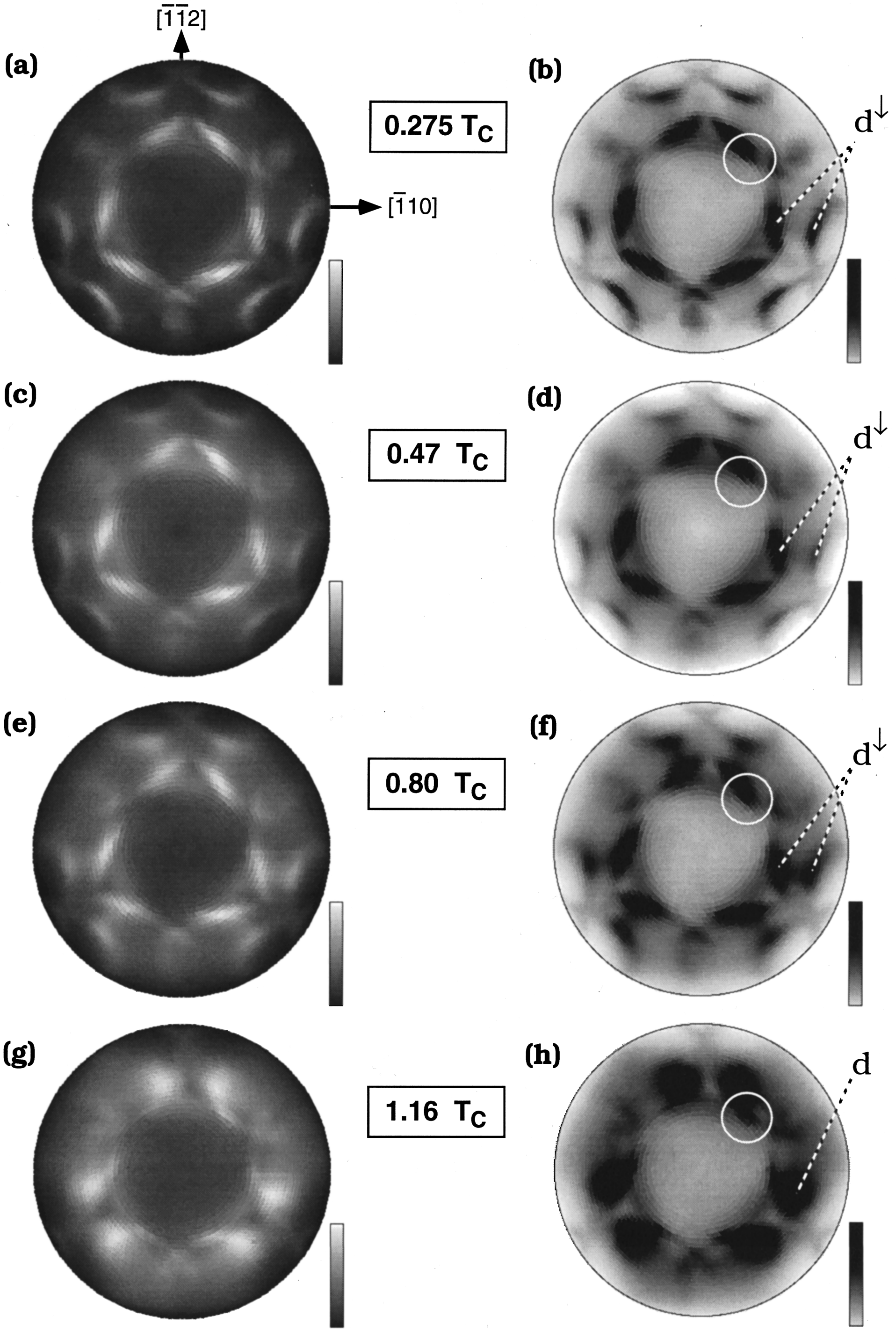

FIG. 5. Fermi-surface maps from Ni(111) taken with monochromatized He I radiation. Sample temperatures and high-symmetry directions are indicated. All data are presented in parallel projection. On the left-hand side the linear grey scale ranges from minimum intensity in black to maximum intensity in white. The same data are displayed on the right-hand side with inverted grey scale and slightly enhanced contrast.

through the (111) surface of nickel at four different temperatures. In Fig. 5 the data are presented in parallel projection (see Sec. II B). The sample temperatures were 162 K for (a) and (b), 297 K for (c) and (d), 503 K for (e) and (f), and 730 K for (g) and (h).

In Sec. III B the temperature behavior of the *sp* bands around the [1 12] direction will be examined in great detail. Here we want to concentrate on the *d* bands at the Fermi level, which are indicated on the right-hand side of Fig. 5 (compare also Figs. 3 and 4). From $0.275T_C$ to $0.47T_C$ no significant changes in the positions of the bands can be detected. This is not surprising. As will be shown in Sec. III C the *d* bands exhibit a Stoner-like temperature behavior, and the macroscopic magnetization changes by only 3.5% within that temperature range.

At $0.8T_C$ [Figs. 5(e) and 5(f)] the two features representing the minority *d*-band move closer to each other. As will become clear in Sec. III C, some of the intensity observed

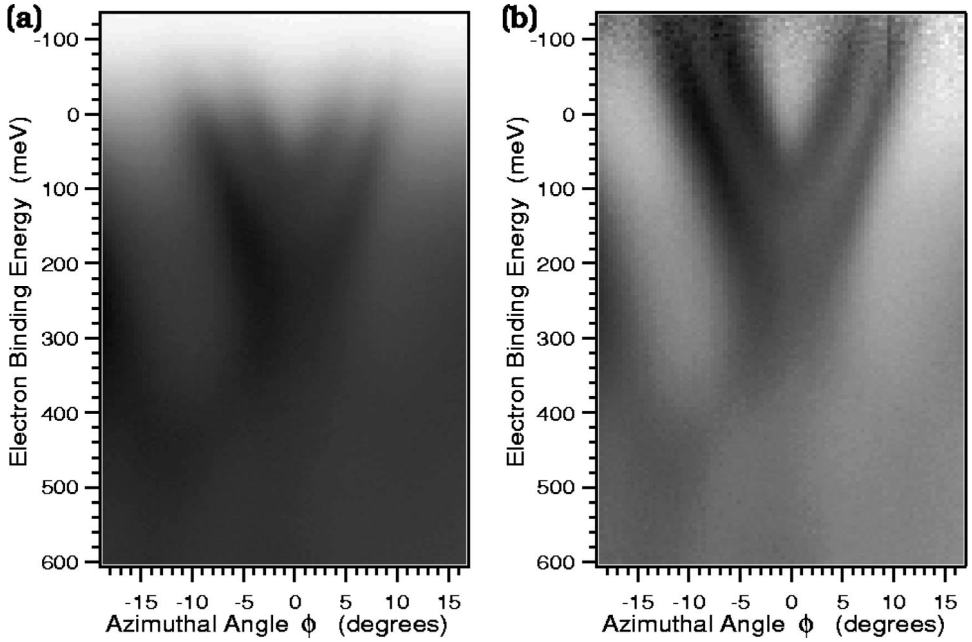

FIG. 6. Azimuthal angle-scanned EDCs taken from Ni(111) at RT and at a polar angle of $\theta_{\mathrm{vac}}=78°$ covering two symmetry-equivalent *sp* bands. The azimuth $\phi=0°$ indicates the [1 12] direction. The raw data are presented in (a), while the data in (b) have been normalized with the ''angle-average'' (compare Sec. II B). The linear grey scale ranges from black at maximum intensity to white at minimum intensity.

between the minority spin features may be attributed to the majority *d* band. Finally, above T_C only one large intensity spot from the *d* band remains, and the spin labels lose their meanings [Figs. 5(g) and 5(h)].

In Ref. 24 the same behavior has been found on the Ni(110) crystal, but one band, which is labeled ''A''' in Fig. 1(b) of Ref. 24, appeared to remain in place upon raising the temperature above T_C. Although we now discuss data taken from the (111) face of nickel, we are examining the same bands in approximately the same location in **k** space. Therefore we should be able to observe the same temperature-independent band here. On the right-hand side of Fig. 5 the white circle surrounds the angular range where this feature appears. For the relation between the Fermi surface as viewed through the (111) and the (110) face see Fig. 3 and Fig. 1 of Ref. 24. Following the temperature development in Fig. 5, we find that indeed a feature of high intensity, centered in the encircled area, appears to remain fixed in **k** space. The same behavior can be seen with varying clarity in all of the six symmetry-related places in the Fermi-surface map. As mentioned above, intensity variations can be ascribed to polarization effects.

In view of our scrutiny of Stoner-like versus noncollapsing exchange-splitting behavior it is important to further investigate the nature of the band that apparently does not move in **k** space with temperature. As will be worked out in Sec. III C, not only *d* bands, but also *sp* bands exist in the area under examination. These steeply dispersing bands are responsible for the observed stationary feature, which nevertheless does not imply a deviation from a Stoner-like behavior, as suggested in Ref. 24.

B. Dispersion and exchange splitting of *sp* bands

In Ref. 34 the exchange splitting of *sp* bands as derived from angle-scanned EDC data at room temperature (RT) from Ni(110) has been discussed. The collapsing exchange-splitting behavior could be clearly deduced from one data set taken at approximately T_C. In this section the temperature dependence of the *sp* bands will be examined in greater detail, analyzing data taken from the Ni(111) crystal surface.

In the Fermi-surface map presented in Fig. 3(c) the exchange-split *sp* bands appear six times due to the $3m$ symmetry of the pattern, always at high polar angles near the [1 12]-equivalent directions. The best way to study their angular splitting through the (111) face is to take azimuthal scans in the vicinity of the [1 12] direction at a high polar angle, e.g., $\theta_{\mathrm{vac}}=78°$. As already discussed in Sec. III A and indicated in Fig. 3(d), the corresponding **k**-space location approximately coincides with the one examined in Ref. 34.

Figure 6 shows angle-scanned energy distribution curves around the [1 12] azimuth ($\phi=0$) taken at room temperature ($0.47T_C$) and with the polar angle fixed at $\theta_{\mathrm{vac}}=78°$. The EDCs cover the range from 130 meV above the Fermi level to $E_{\mathrm{bind}}=600$ meV in steps of 5 meV and are taken every 0.43° in ϕ. Figure 6(a) shows the raw data, whereas in (b) the ''angle-averaged'' data (compare Sec. II B) are presented for visualization of intensities above E_F. Due to the mirror symmetry we see the exchange-split pair of *sp* bands two times near the [1 12] direction. The slight difference in intensities left and right from [1 12] is ascribed to polarization effects mentioned before. The intensity between 200- and 400-meV binding energy near $\phi=-15°$ stems from the minority *d* band (confer Fig. 3) and will not be discussed here.

In analogy to the analysis in Ref. 34 the data have been examined by a peak fitting procedure. The angular distribution curves were fitted with four Gaussian peaks and a linear background. The peak positions give the dispersion of the *sp* bands along the azimuthal scan. In the range $E_F\pm 80$ meV the dispersions of the four observed bands are linear and coincide within 10%, yielding 42.25 ± 4.1 meV/degree. The

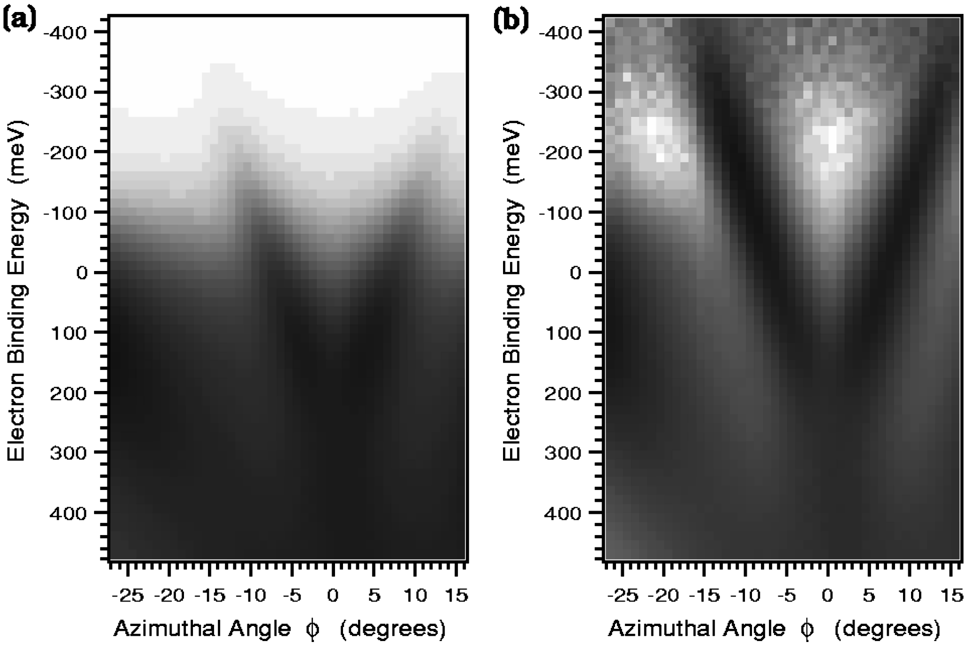

FIG. 7. Same as Fig. 6, but data taken at a sample temperature of $1.146T_C$.

angular exchange splitting at the Fermi level is 4.84° ±0.09°, from which the energetic exchange splitting $\Delta E_{\mathrm{ex}} = 205 \pm 20$ meV can be calculated. This value is in excellent agreement with the result in Ref. 34, where $\Delta E_{\mathrm{ex}} = 204 \pm 8$ meV was found for the *sp* bands. This confirms that we investigate in both cases the same initial-state bands at approximately the same location in **k** space (compare Sec. III A and Fig. 3), although here we are taking data from Ni(111), and in Ref. 34 data from the (110) face of nickel. This also demonstrates the high quality of the data and the reproducibility of the experiment.[44]

A similar data set as that of Fig. 6, but taken at a temperature of 723±9 K, i.e., $T = (1.145 \pm 0.01)T_C$, is presented in Fig. 7. The raw data are shown in (a), while (b) is the grey scale representation of the Fermi-function normalized data. As in Ref. 34, a clearly Stoner-like behavior of the *sp* bands can be observed. Above T_C the formerly exchange-split *sp* bands collapse to one *sp* band. Analyzing the data by fitting two Gaussian peaks on a linear background to the ADCs yields a linear dispersion of 45.6±0.7 meV/degree in the range from 140 to -300 meV binding energy. This compares well to the RT value of 42.25±4.1 meV/degree, and we found that the high-temperature *sp* band lies almost centered between the RT bands as in Ref. 34.

With this knowledge we can study the temperature dependence of ΔE_{ex} by recording one angular distribution curve per temperature, which is one or two orders of magnitude faster than taking a full set of angle-scanned EDCs. At about 30 different temperatures between 119 K ($0.19T_C$) and 838 K ($1.33T_C$) ADCs at the Fermi energy were recorded in azimuthal steps of 0.29° near the $[1\,12]$ direction. As in the angle-scanned EDCs above, the polar angle was fixed at $\theta_{\mathrm{vac}} = 78°$. In order to avoid systematic errors the data were measured in three sets, each time taking ADCs both at increasing and at decreasing temperatures. As already mentioned in Sec. II A measurements at elevated temperatures could be taken during rather long periods of time, because the main contamination, CO, desorbs from the sample surface already at about 450 K. Some of the raw data are presented in Fig. 8(a).

Obviously the exchange-split bands do not collapse abruptly, but move towards each other slowly and continuously when raising the temperature. For a quantitative analysis, the ADCs were fitted with four Gaussian peaks on a linear background, taking advantage of the symmetry in order to decrease the number of fitting parameters. Only up to $T \leqslant 0.83T_C$ the two exchange-split bands can be fitted and separated, while above this temperature basically one single peak on each side of the $[1\,12]$ direction remains in the ADCs. Possibly a more advanced fitting method, like the maximum entropy regularization,[45] would work up to slightly higher temperatures.

As the peak-fitting procedure is limited to the data taken at temperatures well below T_C, we also analyzed the data by simply determining the angular FWHMs. At high temperatures this is the width of the one remaining *sp* peak, and at lower temperatures it is the FWHM of the double-peak consisting of both the majority and the minority *sp* band. These values are presented in Fig. 8(b). The straight line in (b) is fitted to the values clearly above T_C, which show a slowly increasing FWHM with temperature. Subtracting this line from the data points in order to remove thermal broadening effects and the offset due to the single peak width yields the data shown in Fig. 8(c). The solid line in (c) is the bulk magnetization curve as derived from the molecular field theory, rescaled to fit the data points below T_C.

The experimental data represent a microscopic measure of the magnetization and follow the tendency of the macroscopic bulk magnetization rather well, but the agreement is not perfect. The definition of the FWHM may be a source of systematic errors, in particular because the maximum height of the double-peak at low temperatures is always the height of the minority *sp* peak. At the lowest temperatures the manipulator performance might have been a problem. The ori-

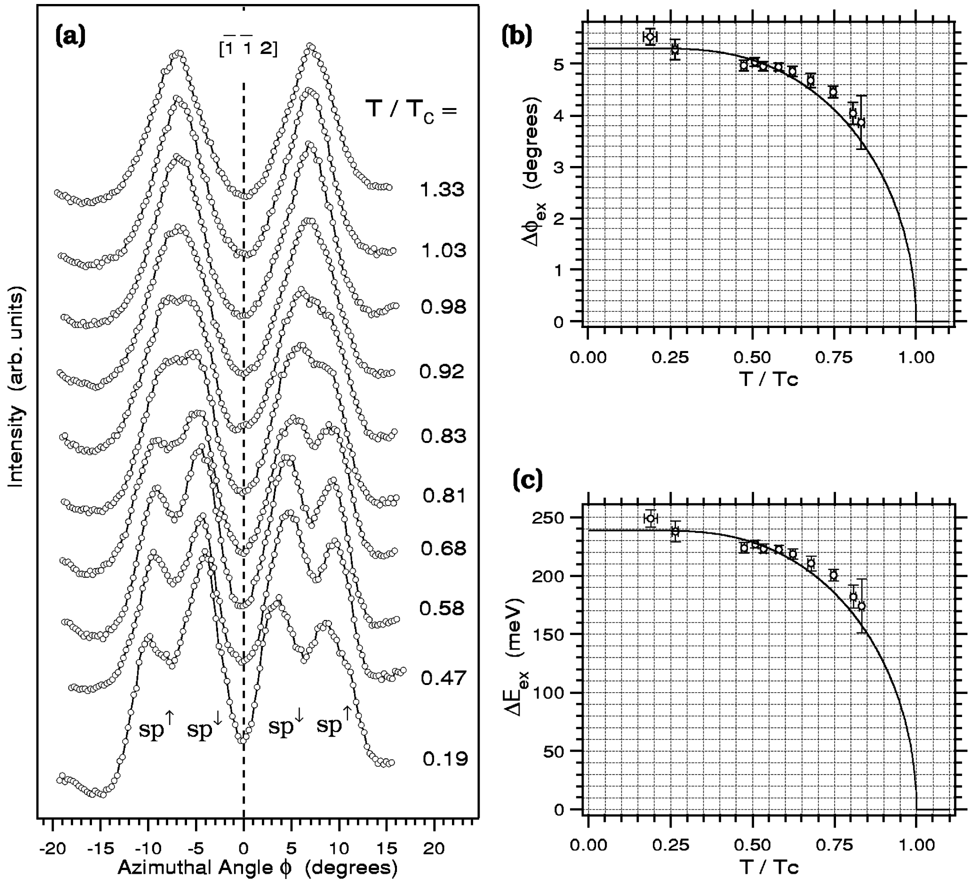

FIG. 8. Temperature-dependent exchange splitting of *sp* bands. In (a) azimuthal Fermi-level ADCs taken at various temperatures from Ni(111) with $\theta_{\mathrm{vac}}=78°$ are presented. In (b) the FWHM of the single *sp* peak (at high temperatures) and of the double peak of the exchange-split pair of *sp* bands (at low temperatures) is plotted vs the temperature. Subtracting the high-temperature fitted straight line in (b) from the data points to remove thermal broadening effects and the intrinsic width yields the data in (c). The solid line in (c) is the bulk magnetization curve rescaled to best fit the data.

gin of the deviations above $0.65T_C$ is not clear. Also in earlier work using spin-resolved PES (Refs. 22 and 46) the temperature dependence of ΔE_{ex} in nickel has been compared to the bulk magnetization curve. There it has been found that the experimental values for temperatures near T_C tend to lie below the curve. This has been interpreted in terms of a reduced magnetic moment within the top surface layers. Calculations for the (110) surface of nickel by Wang[47] have predicted a faster decreasing magnetization for three atomic layers than for the bulk. Therefore our results may confirm the observation of surface effects in the ARUPS experiments. But it should be noted that in both studies cited above[22,46] the data were taken with poor angular resolution, which can lead to ambiguous results. Nevertheless, in a newer spin-resolved study[48] of the ‘‘6 eV satellite’’ in nickel,[20] a similar temperature behavior as in the other two studies was found. The quantity that has been compared to the macroscopic magnetization curve is the height of a dip profile fitted to the photon-energy dependent polarization signal, which was interpreted as a measure for local magnetic moments.

C. Dispersion and exchange splitting of *d* bands

While the exchange-split pair of bands examined in the last section could be clearly identified as fast-dispersing *sp* bands, we now focus on a region in **k** space where the magnetic *d* bands can be observed.

The data discussed in this section are angle-scanned EDCs (confer Sec. II B). The first data set, shown in Fig. 9, is measured at room temperature in steps of 1° from $\theta_{\mathrm{vac}}=76°$ to normal emission on an azimuth 67° off the [110] direction and 23° off [1 12], also indicated in Fig. 3(d) as ‘‘PS1.’’ The energy spectra range from $E_{\mathrm{bind}}=550$ meV to -150 meV in steps of 10 meV, thus crossing E_F. In Fig. 9(a) the raw data are presented. Two bands of similar parabolic dispersion can be identified. The intensity drop above E_F, associated with the Fermi-Dirac distribution function, cuts the apex of the upper band. The Fermi-function normalized data (see Sec. II B) are shown in Fig. 9(c). Here the closed parabola of the upper band is nicely recovered. From these data alone one can identify the two bands as two exchange-split *d* bands. In Sec. III A it has been shown that this assignment is unambiguous. From fitting parabolas to the data, as shown by the dashed lines in the maximum-contrast normalized data in 9(b), an exchange splitting of 280 ± 20 meV is deduced. This is compatible with *d*-band exchange splittings from ARUPS experiments reported in the literature,[39,49–51] where values between 170 and 330 meV were obtained. The apexes are at $\theta_{\mathrm{vac}}=41°\pm 2°$ or $k_{\parallel}=1.344\pm 0.054$ Å^{-1}.

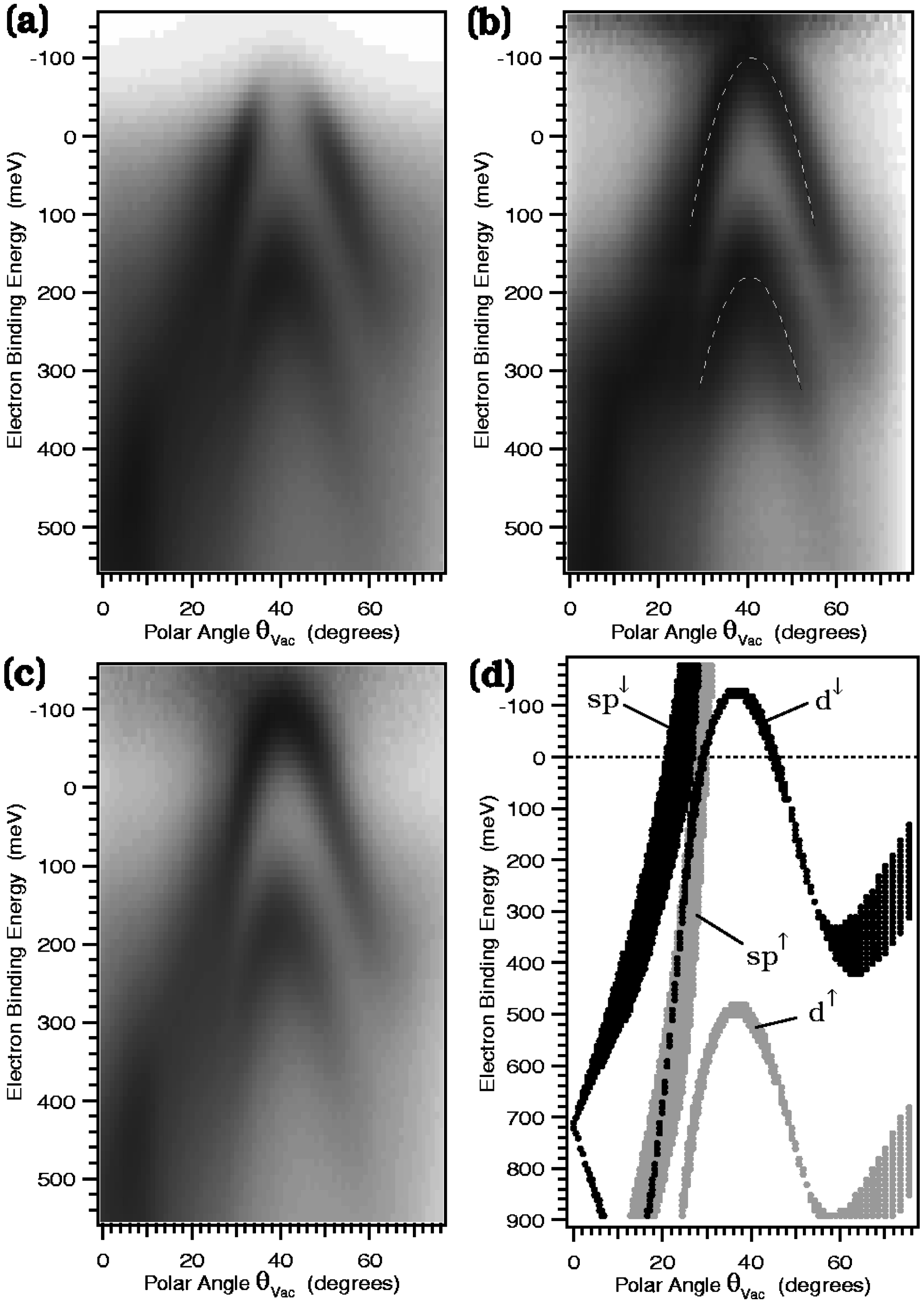

FIG. 9. Angle-scanned EDC data taken at RT from Ni(111) along a section in **k** space denoted ''PS1'' in Fig. 3(d). (a) shows the raw data, (b) and (c) display the data, normalized with the maximum-contrast normalization and with the Fermi function, respectively. The linear grey scale ranges from black at maximum intensity to white at minimum intensity. (d) shows a LKKR calculation corresponding to this section in **k** space. Note that the energy scale is different in (d).

Slight modification of the band-structure code[38] described in Sec. III A permits the calculation of angle-scanned EDC type data taking into account the variation of the final state circle radius with the initial state binding energy. Figure 9(d) shows such a calculation for the polar scan under discussion. Grey markers represent majority bands and black markers bands of minority spin.

In these calculations the Green-function scattering formalism finds $k_\perp$ eigenvalues for a given $k_\parallel$ and a given energy. If the value of such a $k_\perp$ differs by less than 0.04 a.u.$^{-1}$ from the $k_\perp$ expected for a free electron final state, the $k_\parallel$-E pair is written into the output. The spin dependence is explicitly incorporated into the calculations by an exchange term (compare Ref. 52). The results shown in Fig. 9(d) are such $k_\parallel$-E pairs.

Comparing these results to the experimental data [Figs. 9(a)–9(c)], we find a generally good agreement. For a better comparability of theory and experiment the LKKR data are plotted against the polar angle in vacuum θ_{vac} (Ref. 53) and the energy scale is compressed, so as to roughly match the effective masses of the bands. It is well known that band calculations, not explicitly incorporating electron correla-

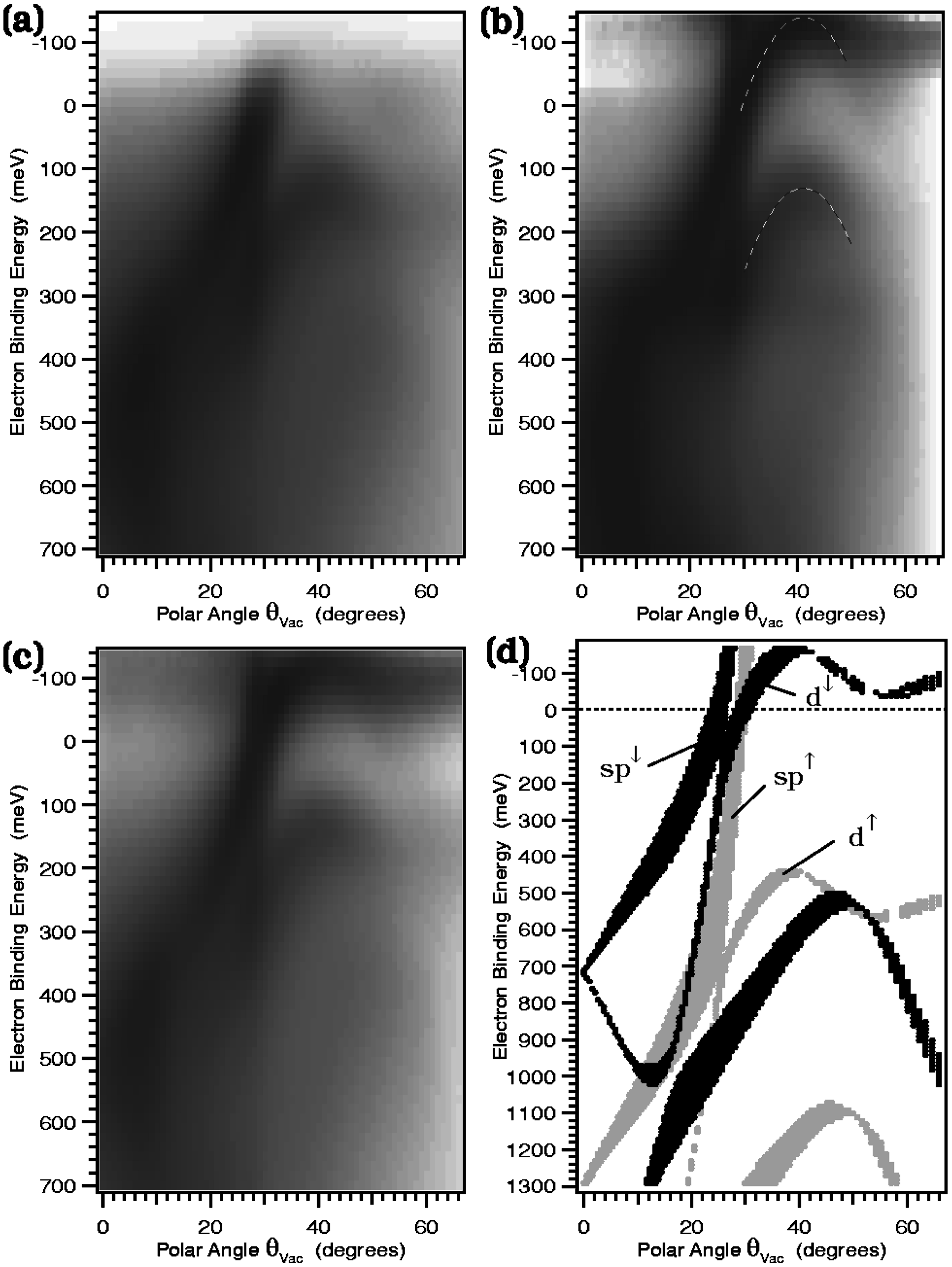

FIG. 10. Same as Fig. 9, but along a section in **k** space denoted ''PS2'' in Fig. 3(d).

tions, overestimate band widths.[54,55] Also the exchange splitting of 620±20 meV as derived from the LKKR results is too large. As the dispersion of the *d* band near the apex is approximately parabolic [see Figs. 9(b) and 9(d)], we can determine the projected effective masses m^* of the electrons both in the experiment and in the LKKR calculation. For the ratio of the two we obtain $m^*(\mathrm{LKKR})/m^*(\mathrm{Expt.})=1.91 \pm 0.20$. Within the error bars this value coincides with the ratio of the exchange splittings $\Delta E_{\mathrm{ex}}(\mathrm{LKKR})/\Delta E_{\mathrm{ex}}(\mathrm{Expt.}) = 2.21 \pm 0.17$. This is reasonable, since in a first approximation the incorporation of correlation effects in band-structure calculations for metals can be understood as a renormalization of the kinetic energy scale, which therefore alters band separations and band curvatures to the same extent.

The *d*-band maximum at $\theta_{\mathrm{vac}}=37° \pm 2°$ is quite close to the experimentally found value of $41° \pm 2°$, but it should be noted that the angle scale in Fig. 9(d) is based on the assumed inner potential $V_0=10.7$ eV (Ref. 39) and the work function $\Phi=5.22$ eV,[40] which were taken from the literature without further adjustment. The complicated situation near $E_{\mathrm{bind}}=280$ meV and $\theta_{\mathrm{vac}}=18°$ seen in the experimental data has its reason in the two exchange-split *sp* bands that touch and even cross the *d* band in this region. Extracting the angular distribution curves between 180- and 380-meV binding energy allows the identification of three bands dispersing in that area (not shown), but for a clear identification the situation is too complex. The fact that the broad features at higher polar angles in the calculation are not very clearly visible in the experiment is partially due to the fact that in the experiment the intensity decreases strongly with θ_{vac} above 60° or 70°.

Figure 10 shows, in complete analogy to Fig. 9, a polar

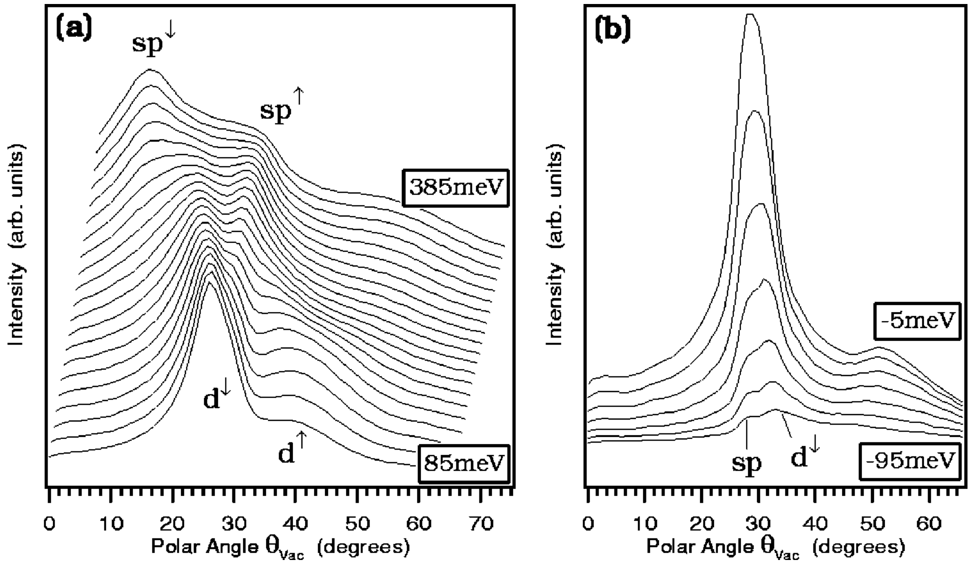

FIG. 11. Angular distribution curves extracted from the data shown in Fig. 10. For clearer visibility the ADCs in (a) are offset in intensity and in θ_{vac} (by 0.4°/15 meV). The highest and lowest electron binding energies are indicated near the corresponding ADC.

scan of spectra that are taken in θ_{vac} steps of 1° from 66° to 0° and in the energy range from 700 meV below to 135 meV above E_F in steps of 15 meV. The azimuthal direction is 53° off$[\bar{1}10]$ and 37° off $[\bar{1}\bar{1}2]$. In Fig. 3(d) the azimuthal direction of the polar scan is indicated as ''PS2.''

The exchange splitting of 270 ± 20 meV that can be extracted from this set of data is hardly differing from the value obtained from Fig. 9, which is reasonable, since we are studying the same bands not very far apart in **k** space. Yet the bands moved up in energy by about 45 meV and by 2° to a higher polar angle. In the LKKR calculations ΔE_{ex} amounts to 600 ± 30 meV, which is also only slightly smaller than what was obtained from Fig. 9(d). Accordingly the ratio of these two exchange splittings $\Delta E_{\text{ex}}(\text{LKKR})/\Delta E_{\text{ex}}(\text{Expt.}) = 2.22\pm0.22$ is practically the same as for the data in Fig. 9. The ratio of the projected effective masses near the apex of the d band, determined from fitting parabolas as described before, yields the value $m^*(\text{LKKR})/m^*(\text{Expt.}) = 1.45 \pm 0.39$. Thus for this polar scan the two ratios agree less well than for the scan from Fig. 9, but they still lie remarkably close.

Furthermore we find that the sp bands moved away from the minority d band by some degrees, as can also be seen in the LKKR calculation of Fig. 10(d). This allows one to distinguish the three bands $sp^{\uparrow}$, $sp^{\downarrow}$, and $d^{\downarrow}$. As suggested by the experimental data as well as by the LKKR calculation of Fig. 10(d) the band with the steepest dispersion measured between -100 and 300-meV binding energy can be associated with the the majority sp band. Near $E_{\text{bind}} = 200$ or 300 meV the three bands cross each other and can experimentally be discriminated rather well, as is clearly shown in Fig. 11(a), where the ADCs from 85-to 385-meV binding energy are presented. Including the $d^{\uparrow}$ band, four distinct bands can be found in this figure. Also above the Fermi level the separation of the $d^{\downarrow}$ band from the sp bands can be detected. This is visible in the grey scale representation of the data [Fig. 10(c)] and in the ADCs extracted in the range $E_{\text{bind}} = -95$ meV to $E_{\text{bind}} = -5$ meV in Fig. 11(b).

So far we have discussed the dispersion and the exchange splitting of d bands at room temperature. In the two angle-scanned EDC data sets of Fig. 9 and Fig. 10 the observed direct transitions could be unambiguously assigned to initial states from d and sp bands, strongly supported by our LKKR calculations. Based on this knowledge we now want to study the behavior of the d bands during the magnetic phase transition.

Figure 12 displays polar-angle scanned energy distribution curves taken along the same azimuthal direction as the data in Fig. 9. On the left-hand side the raw data are presented, and on the right-hand side the data have been normalized with the Fermi function (see Sec. II B). Angular steps of 1° and energy steps of 10 meV were taken. The respective ranges can be inferred from the figure.

The data in Figs. 12(a) and 12(b) were taken at room temperature $(297\,\text{K} = 0.47Tc)$.[56] The overlap of the d and sp bands near E_F is strong and does not allow to distinguish them in the experiment. At room temperature the Fermi step is steep and does not populate states at energies far enough above the apex of the minority d band so as to be able to observe the strongly dispersing sp bands there.

In Figs. 12(c) and 12(d) the data taken at 507 K $= 0.80T_C$ are presented. The d bands have moved towards each other leading to a decreased exchange splitting. In analogy to Fig. 9(b) parabolas have been used to determine ΔE_{ex} for this case. A value of $\Delta E_{\text{ex}} = 210\pm20$ meV could be deduced. The fact that the minority d band moved down towards E_F, and that the Fermi edge is broader at this higher temperature, now allows one to see the above-mentioned sp bands. At 150 or 200 meV above E_F the sp band is found at $\theta_{\text{vac}} = 31°$.

Above the Curie temperature the exchange splitting of the d bands has vanished, as can be concluded from the data presented in Figs. 12(e) and 12(f), taken at 766 K $= 1.21T_C$. Only a single d band remains. The energy width of this band is larger than the widths at the lower temperatures. Near the apex the FWHM is 190 ± 15 meV as derived

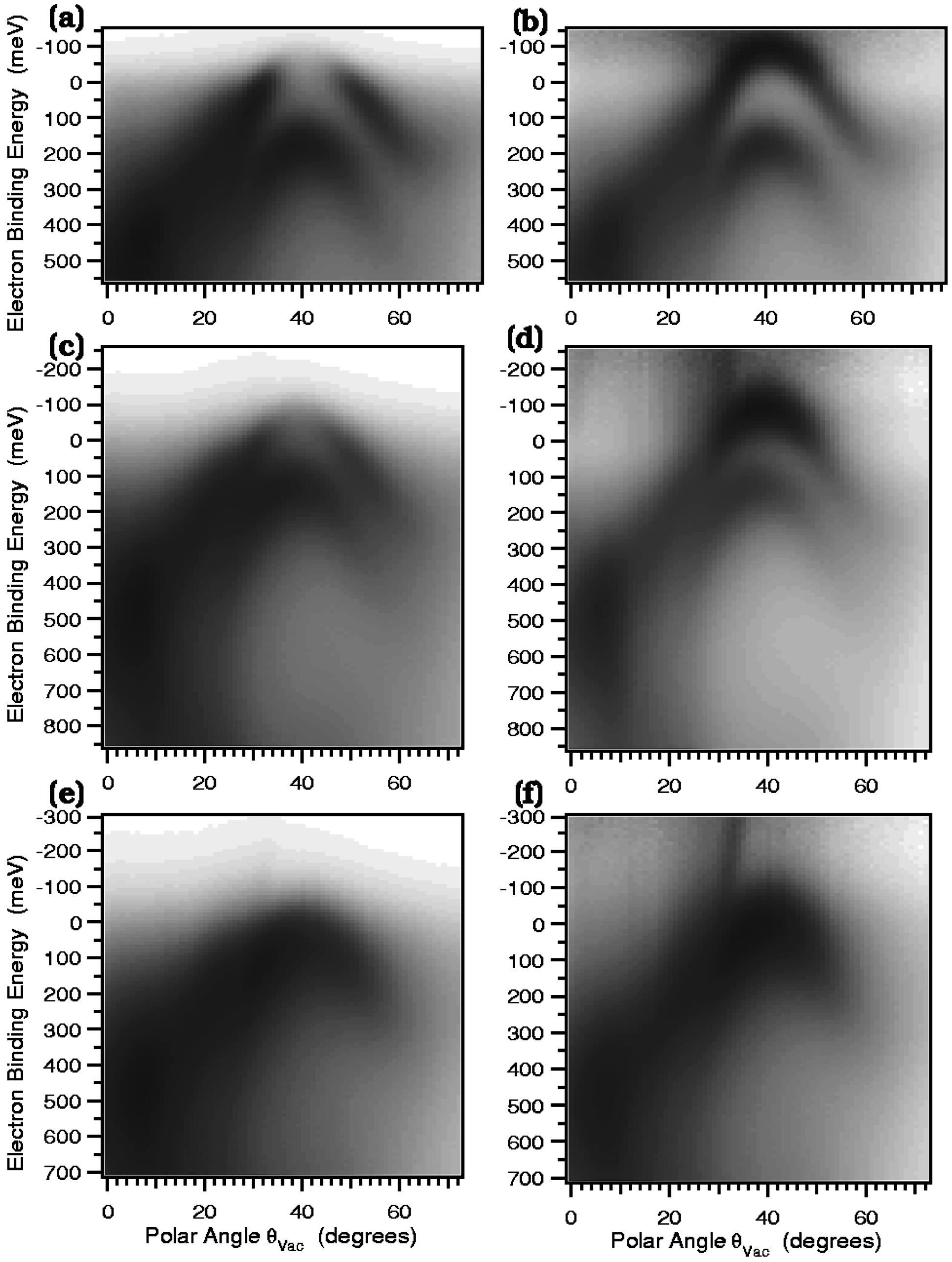

FIG. 12. He I-excited polar-angle scanned EDCs taken from Ni(111) along the same azimuth as the data shown in Fig. 9 [''PS1'' in Fig. 3(d)], measured at three different temperatures. Raw data are presented on the left, the Fermi-function normalized data (see Sec. II B) are given on the right. The linear grey scale ranges from minimum intensity (white) to maximum intensity (black). The sample temperatures were $0.47T_C$ in (a) and (b), $0.80T_C$ in (c) and (d), and $1.21T_C$ in (e) and (f).

from the Fermi-normalized data, while at $0.80T_C$ 135 ± 20 meV and at $0.47T_C$ 110 ± 15 meV were found. This broadening can be partially attributed to the increased electron-phonon interaction at higher temperatures. For the Cu(111) surface state the temperature-dependent peak broadening has been examined by McDougall and co-workers,[57] yielding a value of 0.074 meV/K in the temperature range from 30 to 625 K. Applying this value to our measurements on nickel can account for about 50% of the observed broadening effects.

The peak widths in EDCs depend on the lifetimes and on the group velocities of the initial and final electron states.[58] Therefore, changes in these quantities could be the reason for the larger linewidth at elevated temperatures. But the data (Figs. 12 and also 13) imply a rather rigid behavior of the bands, which means that the group velocities are approximately the same below and above T_C. Also the quasiparticle lifetimes, if they can be described by the Fermi liquid theory,[59] cannot explain the findings: At any of the temperatures the *d* bands were examined within the same small energy range of $E_F \pm 150$ meV (see Fig. 12), and above T_C the *d* band even lies right at the Fermi level, where lifetimes are longest and linewidths are smallest. In the simple Stoner picture[3,4] the bands are rigidly shifted versus each other with increasing temperature. But they remain unchanged otherwise, not allowing for an additional broadening. Therefore, this is another experimental indication that the simple Stoner model does not properly describe the phase transition.

Not only the linewidths, but also the peak intensities, show an unexpected behavior. As discussed in Ref. 28 there is a clearly enhanced intensity of the minority d band relative to the majority d band in the normalized data (compare our Fig. 12 and Fig. 4 of Ref. 28). This is not an artifact of the normalization procedure, and we get the same result using the angle-average normalization (compare Sec. II B). The intensity difference is unlikely to be caused by matrix element effects because of the close proximity of the bands in energy and in **k** space. A spin-dependent matrix-element effect is ruled out by our experimental setup, since the average sample magnetization is zero and weakly linearly polarized light is used.

We therefore interpret the high intensity of the emission from the minority d band to be caused by the strong interaction with the nearby sp band. In Fig. 12(f) this sp band can be seen even clearer than in (d). In the range from -100 to -300 meV (above E_F) there is only little intensity from the minority d band left, allowing one to detect the weak sp intensity. New important aspects concerning the magnetic phase transition in nickel are provided by these data: We monitor a region in **k** space where the minority d band and the exchange-split pair of sp bands cross the Fermi level at the same **k** and with nearly the same group velocity. This means that minority electron transitions of the type $sp \rightarrow d$ may be strong, which could reduce the Stoner gap, usually associated with d-electron transitions from majority to minority, to zero.

The minority sp band could therefore act as an electron reservoir that populates the minority d band already before the minority d band is depopulated when the temperature is raised. This leads to a reduced magnetic moment and a decreased ΔE_{ex}, thus supplying a positive feedback driving the phase transition. And, as suggested by the high relative intensity of minority to majority d electrons, the occupation number of the minority d electrons could be higher than expected.

Furthermore it is interesting to note that the d-band peak above T_C lies precisely at E_F. Therefore we located a **k** vector where spin flips would cost no energy, making our data fully consistent with fluctuating local moments and spin waves in the paramagnetic state. The anomalously large linewidth in the data of Figs. 12(e) and 12(f) might even be a consequence of these.

We now again move slightly away to a location in **k** space, where the sp band is separately detectable already at room temperature. The RT data of the polar scan 53° off [110] and 37° off [1 12] (compare Fig. 3, ‘‘PS2’’) have already been discussed in Fig. 10. Figure 13 displays angle-scanned EDCs taken along this same azimuth and measured at different sample temperatures.[60] As in Fig. 12 the left-hand side shows the raw data and the right-hand side the normalized data. For the lowest temperature of 139 K $=0.22T_C$ the ‘‘angle-average’’ normalization [Fig. 13(b)] has been applied to the raw data [Fig. 13(a)], while the data in (d) at 297 K$=0.47T_C$ and in (f) at 689 K$=1.09T_C$ have been normalized with the Fermi function.

In conjunction with the LKKR calculations [Fig. 10(d)] the existence of an exchange-split pair of sp bands has been deduced and confirmed by the RT data (see also Figs. 10 and 11). As also shown before the exchange splitting of the d band, which is here no longer simply parabolic, amounts to $\Delta E_{\mathrm{ex}} = 270 \pm 20$ meV at room temperature. With $\Delta E_{\mathrm{ex}} = 300 \pm 40$ meV derived from the data in (b) the splitting at $0.22T_C$ is slightly larger. The estimated error of 40 meV has its origin in the weak definition of the minority d band, which has its apex approximately 160 meV above the Fermi level. This is clearly outside the range of $5k_BT$ above E_F, where we can currently measure reliable band dispersions in our experiment.

Above T_C [Figs. 13(e) and 13(f)] the collapsing band behavior of the d bands manifests itself again in a single high-temperature band. As in the data of Fig. 12(e) and 12(f) the two d bands meet at E_F and we observe an increased linewidth. Also here the minority to majority d-intensity ratio is anomalously large below T_C. Since the sp and the minority d band lie equally close to the Fermi level as in the data of Fig. 12, these findings can be explained along the same line, involving the importance of minority sp-d interaction.

Since the Fermi step is broad in the data taken at $1.09T_C$, the sp band can be clearly identified between -100 meV and -300 meV (above E_F), dispersing with a high group velocity (Fig. 13). The dispersion of the sp band can be quantified, yielding about 125 meV/degree. Assuming a room-temperature exchange splitting of the order of 200 meV (compare Sec. III B) an angular exchange splitting of only some 1.6° at low temperatures is expected. Therefore it is clear that at room temperature the sp-band exchange splitting cannot be detected in this **k**-space region by our experiment. Only explicitly spin-resolved measurements with high angular resolution could resolve these bands.

On this basis we can understand the apparently stationary behavior of this band, which has suggested deviations from a simple Stoner-like behavior, as reported in Ref. 24. The band that remains apparently unchanged and fixed in **k** space as observed in the Fermi-surface maps in Fig. 1 of Ref. 24 and Fig. 5 (Sec. III A) is actually composed of a spin-split pair of sp bands with high group velocities, which are not resolved due to their small angular exchange splitting.

Since the data sets of Figs. 12 and 13 present the same d band in a similar location in **k** space and accordingly show about the same exchange splitting, we can plot all the derived d-band exchange splittings versus the temperature. Figure 14 shows the resulting temperature dependence of d bands. The solid line is the macroscopic bulk magnetization curve scaled to fit the experimental data. As in the case of the sp bands (Sec. III B) we find a generally good agreement of the exchange splitting ΔE_{ex} with the macroscopic bulk magnetization behavior. It should again be noted that ΔE_{ex} is a microscopic quantity describing the magnetism, but in the ARUPS experiment it is averaged within the macroscopic area of electron detection on the sample. The ground-state exchange splitting derived from the fit is 290 ± 10 meV.

IV. CONCLUSIONS

The temperature-dependent electronic structure of nickel near the Fermi energy has been studied by angle-resolved ultraviolet photoelectron spectroscopy. New and unconventional modes of data acquisition in ARUPS, specifically

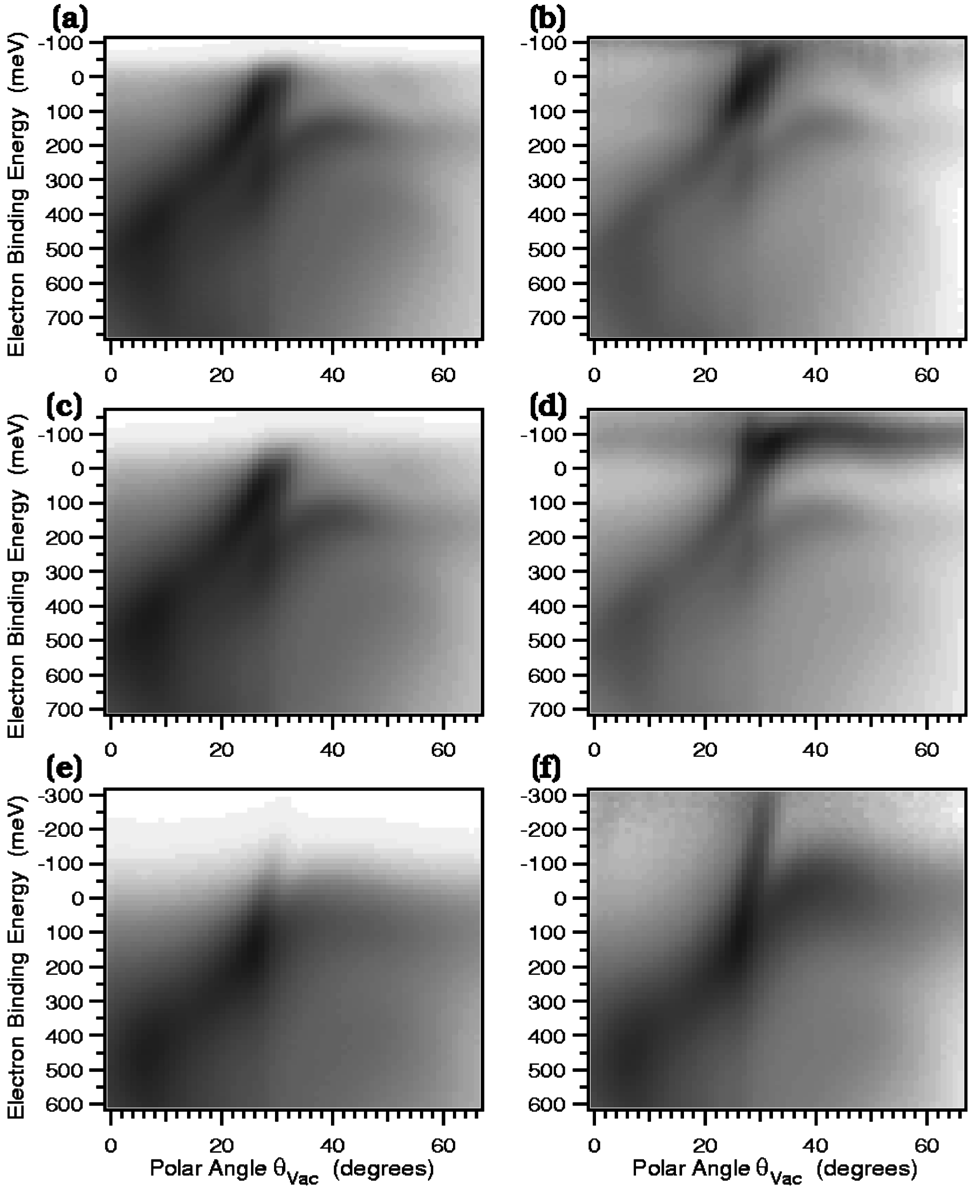

FIG. 13. He I-excited angle-scanned EDCs taken from Ni(111) along the same azimuth as the data shown in Fig. 10 [''PS2'' in Fig. 3(d)], taken at three different temperatures. Raw data are presented on the left, normalized data on the right. The linear grey scale ranges from minimum intensity (white) to maximum intensity (black). The sample temperatures were $0.22T_C$ in (a) and (b), $0.47T_C$ in (c) and (d) and $1.09T_C$ in (e) and (f).

constant-energy surface maps, angular distribution curves (ADCs), and angle-scanned energy distribution curves, were applied and turned out to be very valuable extensions to the more conventional type of ARUPS data (see Sec. II B). The power of these new methods becomes particularly clear near the Fermi level, and exactly the electrons near the Fermi level are those responsible for the magnetic properties of nickel. Even the thermally excited states up to $5k_BT$ above E_F can be readily analyzed in angle-scanned EDCs (see Secs. III B and III C).

The enhanced effective resolution provided by the new ARUPS modes made a detailed study of the magnetic phase transition possible for both, d and sp electrons. This was only possible because the bands are clearly separable in angular distribution curves, even without explicit spin detection. The extensive temperature dependence study in Sec. III B reproduced the value of $\Delta E_{ex}=204\pm 8$ meV (Ref. 34)

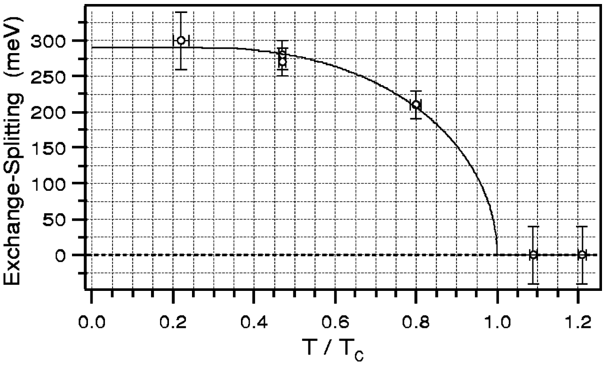

FIG. 14. Temperature dependence of the exchange splitting of d bands. The values are derived from the data in Figs. 12 and 13. The solid line represents the macroscopic bulk magnetization curve scaled to fit the experimental data.

for the sp bands at room temperature with high accuracy. And, more importantly, it revealed a clear Stoner-like decrease of the exchange splitting. The d bands showed this type of temperature behavior as well (Sec. III C). Their RT exchange splitting is larger and amounts to $\Delta E_{\mathrm{ex}}=275\pm 20$ meV.

An anomalously high intensity ratio of the minority to majority d electrons has been observed where sp and d bands coincide on the Fermi surface with nearly the same group velocity. We are convinced that this allows for a strong sp-d interaction and reveals a driving force for the magnetic phase transition. The sp band serves as an electron reservoir for the minority d electrons, and the minority d-band single-particle states can be populated to a higher extent than expected. The observed large linewidth of the paramagnetic d band at the Fermi level is fully compatible with spin fluctuations above T_c and cannot be explained by thermal effects alone.

Constant-energy surface maps taken near the Fermi energy allow the direct and simultaneous examination of the dispersion of several bands in a wide and continuous two-dimensional part of **k** space. Specific constant-energy surface maps, taken at the Fermi energy at room temperature and above T_c, lead in Ref. 24 to the conclusion that the data could not be explained in a Stonerlike picture: One band appeared to remain at a fixed position in **k**-space during the phase transition.

The presented measurements confirm these findings, but make them again consistent with a Stoner-like behavior of the exchange splitting (Secs. III A and III C), notably with the support of band-structure calculations using the spin-polarized layer Korringa-Kohn-Rostoker formalism. Modifications of the program code permit the calculation of data that can be directly compared to angle-scanned EDCs. Under the assumption of a free-electron final state the calculations agree excellently with the experiment. It could be shown that the apparently stationary bands are in fact sp bands with a high group velocity. Therefore they show an angular exchange splitting too small to be detected in the experiment, and the band must appear fixed in **k** space.

ACKNOWLEDGMENTS

This work has been supported by the Schweizerischer Nationalfonds. The technical assistance from the mechanical and electrical workshops at the Universities of Zürich and Fribourg are kindly acknowledged. The authors want to thank M. Donath, D. Pescia, H. C. Siegmann, and R. Willis for stimulating discussions, and W. Deichmann, H.-J. Neff, H. Schmid, P. Schwaller, E. Wetli, and J. Wider for their support.

[1] H. Capellmann, J. Magn. Magn. Mater. **28**, 250 (1982).
[2] M. Donath, Surf. Sci. Rep. **20**, 251 (1994).
[3] E. C. Stoner, Rep. Prog. Phys. **11**, 43 (1947).
[4] E. P. Wohlfarth, Rev. Mod. Phys. **25**, 211 (1953).
[5] H. Capellmann, Z. Phys. B **34**, 29 (1979).
[6] A. Ziegler, Phys. Rev. Lett. **48**, 695 (1982).
[7] V. Korenman, J. Appl. Phys. **57**, 3000 (1985).
[8] D. M. Edwards, J. Magn. Magn. Mater. **15–18**, 262 (1980).
[9] D. M. Edwards, J. Magn. Magn. Mater. **45**, 151 (1984).
[10] J. Hubbard, Phys. Rev. B **23**, 5974 (1981).
[11] A. J. Pindor, J. Staunton, G. M. Stocks, and H. Winter, J. Phys. F **13**, 979 (1983).
[12] H. Capellmann, Z. Phys. B **34**, 29 (1979).
[13] V. Korenman and R. E. Prange, Phys. Rev. Lett. **44**, 1291 (1980).
[14] V. Korenman and R. E. Prange, Phys. Rev. Lett. **53**, 186 (1984).
[15] M. Donath and V. Dose, Europhys. Lett. **9**, 821 (1989).
[16] M. Donath (private communication).
[17] W. Nolting, W. Borgiel, V. Dose, and Th. Fauster, Phys. Rev. B **40**, 5015 (1989).
[18] W. Borgiel and W. Nolting, Z. Phys. B **78**, 241 (1990).
[19] W. Borgiel, W. Nolting, and M. Donath, Solid State Commun. **72**, 825 (1989).
[20] S. Hüfner and G. K. Wertheim, Phys. Lett. **51A**, 299 (1975).
[21] C. J. Maetz, U. Gerhardt, E. Dietz, A. Ziegler, and R. J. Jelitto, Phys. Rev. Lett. **48**, 1668 (1982).
[22] K.-P. Kämper, W. Schmitt, and G. Güntherodt, Phys. Rev. B **42**, 10 696 (1990).
[23] P. Genoud, A. A. Manuel, E. Walker, and M. Peter, J. Phys.: Condens. Matter **3**, 4201 (1991).
[24] P. Aebi, T. J. Kreutz, J. Osterwalder, R. Fasel, P. Schwaller, and L. Schlapbach, Phys. Rev. Lett. **76**, 1150 (1996).
[25] J. Kirschner and E. Langenbach, Solid State Commun. **66**, 761 (1988).
[26] H. A. Mook, J. W. Lynn, and R. M. Nicklow, Phys. Rev. Lett. **30**, 556 (1973).
[27] P. Aebi, J. Osterwalder, R. Fasel, D. Naumovic, and L. Schlapbach, Surf. Sci. **307–309**, 917 (1994).
[28] T. Greber, T. J. Kreutz, and J. Osterwalder, Phys. Rev. Lett. **79**, 4465 (1997).
[29] J. M. MacLaren, S. Crampin, D. D. Vvedensky, R. C. Albers, and J. B. Pendry, Comput. Phys. Commun. **60**, 365 (1990).
[30] T. Greber, O. Raetzo, T. J. Kreutz, P. Schwaller, W. Deichmann, E. Wetli, and J. Osterwalder, Rev. Sci. Instrum. **68**, 4549 (1997).
[31] Design of heating electronics by P. Aebi and F. Bourqui; manufacturing by F. Bourqui (University of Fribourg).
[32] S. Hüfner, *Photoelectron Spectroscopy*, 2nd ed. (Springer-Verlag, Berlin, 1996).
[33] J. Osterwalder, T. Greber, A. Stuck, and L. Schlapbach, Phys. Rev. B **44**, 13 764 (1991).
[34] T. J. Kreutz, P. Aebi, and J. Osterwalder, Solid State Commun. **96**, 339 (1996).
[35] A. Santoni, L. J. Terminello, F. J. Himpsel, and T. Takahashi, Appl. Phys. A: Solids Surf. **52**, 229 (1991).
[36] J. Osterwalder, A. Stuck, T. Greber, P. Aebi, L. Schlapbach, and S. Hüfner, in *Vacuum Ultraviolet Radiation Physics*, Proceedings of the 10th VUV Conference, edited by F. J. Wuilleumier, Y. Petroff, and I. Nenner (World Scientific, Singapore, 1993).
[37] J. Osterwalder, Surf. Rev. Lett. **4**, 391 (1997).
[38] J. M. MacLaren, S. Crampin, D. D. Vvedensky, R. C. Albers, and J. B. Pendry, Comput. Phys. Commun. **60**, 365 (1990).
[39] W. Eberhardt and E. W. Plummer, Phys. Rev. B **21**, 3245 (1980).
[40] *Physics of Solid Surfaces*, edited by D. Hellwege, Landolt-

Bornstein, New Series, Group III, Vol. 24, Pt. 6 (Springer, Berlin, 1994).

[41] M. Lindroos and A. Bansil, Phys. Rev. Lett. **77**, 2985 (1996).

[42] For two-dimensional systems V_0 does not play a role since then $k_\parallel$ only depends on Φ.

[43] P. Aebi *et al.*, Surf. Sci. **402-404**, 614 (1998).

[44] Note that the data were taken with two different experimental apparatuses, i.e., with different manipulators, electron analyzers, and UV sources.

[45] *Maximum Entropy in Action*, edited by B. Buck and V. A. Macaulay (Oxford Science Publications, Oxford, 1990).

[46] R. Raue, H. Hopster, and R. Clauberg, Z. Phys. B **54**, 121 (1984).

[47] S.-W. Wang, Solid State Commun. **36**, 847 (1980).

[48] A. Kakizaki, J. Fujii, K. Shimada, A. Kamata, K. Ono, K.-H. Park, T. Kinoshita, T. Ishii, and H. Fukutani, Phys. Rev. Lett. **72**, 2781 (1994).

[49] D. E. Eastman, F. J. Himpsel, and J. A. Knapp, Phys. Rev. Lett. **40**, 1514 (1978).

[50] F. J. Himpsel, J. A. Knapp, and D. E. Eastman, Phys. Rev. B **19**, 2919 (1979).

[51] P. Heimann, F. J. Himpsel, and D. E. Eastman, Solid State Commun. **39**, 219 (1981).

[52] V. L. Moruzzi, J. F. Janak, and A. R. Williams, *Calculated Electronic Properties of Metals* (Pergamon Press, New York, 1978).

[53] The θ_{vac} scaling is actually exact only at E_F, but the deviations in the energy range under inspection are negligible.

[54] A. Liebsch, Phys. Rev. Lett. **43**, 1431 (1979).

[55] L. C. Davis, J. Appl. Phys. **59**, R25 (1986), and references therein.

[56] Actually Figs. 12(a) and 12(b) show the identical data as Fig. 9(a).

[57] B. A. McDougall, T. Balasubramanian, and E. Jensen, Phys. Rev. B **51**, 13 891 (1995).

[58] P. Thiry, Ph.D. thesis, Université Pierre et Marie Curie, Paris (1981) (in French).

[59] D. Pines and P. Nozières, *The Theory of Quantum Liquids* (Benjamin, New York, 1966).

[60] Actually Figs. 13(c) and 13(d) show the identical data as Fig. 10(a).